ARL-TR-9994 • Oct 2024

Challenges in High-Resolution Multidimensional Radar Signal Processing

by Traian Dogaru

NOTICES

Disclaimers

ARL-TR-9994 ● Oct 2024

Challenges in High-Resolution Multidimensional Radar Signal Processing

Traian Dogaru
DEVCOM Army Research Laboratory

REPORT DOCUMENTATION PAGE

1. REPORT DATE	2. REPORT TYPE	3. DATES COVERED START DATE	3. DATES COVERED END DATE
October 2024	Technical Report	10/01/2023	5/31/2024

4. TITLE AND SUBTITLE
Challenges in High-Resolution Multidimensional Radar Signal Processing

5a. CONTRACT NUMBER	5b. GRANT NUMBER	5c. PROGRAM ELEMENT NUMBER

5d. PROJECT NUMBER	5e. TASK NUMBER	5f. WORK UNIT NUMBER

6. AUTHOR(S)
Traian Dogaru

7. PERFORMING ORGANIZATION NAME(S) AND ADDRESS(ES)
DEVCOM Army Research Laboratory
ATTN: FCDD-RLA-LC
Adelphi, MD 20783

8. PERFORMING ORGANIZATION REPORT NUMBER
ARL-TR-9994

9. SPONSORING/MONITORING AGENCY NAME(S) AND ADDRESS(ES)	10. SPONSOR/MONITOR'S ACRONYM(S)	11. SPONSOR/MONITOR'S REPORT NUMBER(S)

12. DISTRIBUTION/AVAILABILITY STATEMENT
DISTRIBUTION STATEMENT A. Approved for public release: distribution unlimited.

13. SUPPLEMENTARY NOTES
ORCID: Traian Dogaru, 0000-0002-1091-4928

14. ABSTRACT
Surveillance radar systems equipped with active electronically scanned antenna arrays (AESAs) typically operate with low spatial resolution. Under these conditions, the data transformation from the radar signal in the frequency, array position, and slow time dimensions to the reflectivity map in the range, angle, and Doppler dimensions is conventionally performed by a 3-D fast Fourier transform. However, the ability to apply this conventional processing scheme relies on certain approximations, the validity of which becomes questionable as we try to improve the radar system's resolution. In this report, we analyze the conditions when the radar measurement dimensions (frequency, array position, and slow time) become coupled, and we point out to the signal processing challenges posed by this coupling in creating the radar reflectivity map. We discuss possible algorithmic approaches to creating a high-resolution reflectivity map with an AESA radar system and illustrate several simple numerical examples.

15. SUBJECT TERMS
radar clutter, ground penetrating radar, radar imaging, radar modeling, synthetic aperture radar, Electromagnetic Spectrum Sciences

16. SECURITY CLASSIFICATION OF: a. REPORT	b. ABSTRACT	C. THIS PAGE	17. LIMITATION OF ABSTRACT	18. NUMBER OF PAGES
UNCLASSIFIED	UNCLASSIFIED	UNCLASSIFIED	UU	32

19a. NAME OF RESPONSIBLE PERSON	19b. PHONE NUMBER *(Include area code)*
Traian Dogaru	(301) 394-1482

STANDARD FORM 298 (REV. 5/2020)
Prescribed by ANSI Std. Z39.18

Contents

List of Figures

1. Introduction

Typical medium- and long-range surveillance radar systems equipped with stationary active electronically scanned antenna arrays (AESA), operating in search mode, map the sensing domain with low spatial resolution, on the order of 50 to 100 m.[1] There are multiple reasons for this design choice: 1) long-range radar sensing favors low-frequency bands (L- and S-band); 2) the very large area to be mapped precludes its partition into very small-size pixels; 3) implementation of fine cross-range resolution at long ranges would require very wide antenna arrays; 4) the signal processing with low-resolution waveforms and antenna beams is simplified; 5) and most targets behave as point targets within a large-size resolution cell, which is optimal for maximizing the signal-to-noise ratio (SNR) and detection performance.

Nevertheless, other radar operational modes besides searching such as tracking, target identification, and fire control could clearly benefit from high-resolution mapping of the sensing domain.[2] In particular, performing effective target identification and classification would typically involve spatial resolution of approximately 1 m or better, which is comparable to the resolution achieved by synthetic aperture radar (SAR) imaging systems,[3,4] which operate with large bandwidths and long apertures. Attempting to implement this kind of resolution in stationary, array-based radar systems operating at medium and long ranges presents multiple challenges, which form the motivation for this investigation.

One may consider the radar domain mapping process as a data transformation from the radar measurement in the frequency, array position, and slow time dimensions to the reflectivity map (RM) in the range, angle(s), and Doppler (velocity) dimensions. In their simplest form, these operations are performed as three separate discrete Fourier transforms (DFTs), implementing the pulse compression, beamforming, and Doppler processing as a 3-D fast Fourier transform (FFT) procedure. However, the ability to apply this conventional processing scheme hinges on certain approximations, which become tenuous as we try to improve the radar system's resolution.

In this study, we establish the resolution limits beyond which the dimensions become "coupled" (in the sense defined in Section 2). In that case, the signal processing involved in the radar RM formation is much more complex, presenting significant computational challenges to a system required to operate in real time. Besides deriving the conditions for dimensional coupling in the radar measurements, we discuss existing approaches and algorithms designed to handle the processing in these scenarios. In this work, we limit our numerical example to simple computer simulations involving point targets, for the purpose of illustrating the theoretical analysis. More complex and realistic sensing scenarios will be presented in a forthcoming publication.

This report is organized as follows. In Section 2, we introduce the array-based radar system under investigation and establish the coupling criteria between radar measurement dimensions as a function of the system resolution. In the same section, we present a brief account of the strategies and algorithms designed to handle the RM formation in the coupled case. Several numerical examples are shown in Section 3. We draw conclusions in Section 4.

2. Theoretical Analysis of Dimension Coupling in Radar Sensing

2.1 System Configuration and Reflectivity Map Formation

In this investigation, we consider an AESA system equipped with a uniform linear array (ULA) as depicted in Fig. 1. There is one transmitter (Tx) placed in the array's center (also the coordinate system origin), and several receivers (Rx) placed at regular intervals along the array's width, w_A. All the antenna elements are assumed to have omnidirectional patterns in the $x > 0$ half-plane. The Tx sends out a train of identical pulses that are scattered by the target and collected back by each Rx element. The received signals are down-converted and digitized and go through the following processing steps: pulse compression, Doppler processing, and digital beamforming. In the end, the goal is to obtain a RM of the scene in the following coordinates: range, azimuth, and velocity (note that we ignore the elevation dimension in this study; resolving the RM in elevation would require a 2-D antenna array).

The array configuration in Fig. 1 was chosen primarily to simplify the theoretical analysis. Note that practical AESA systems may entail more complex designs, involving multiple Tx elements that perform beamforming and scanning on transmit as well.[1,5] For those scenarios, the coupling relationships established in this work may have to go through some adjustments, typically by some small factors. However, the main thesis proposed by this investigation—that simultaneously trying to improve the resolution in the three dimensions significantly complicates the radar signal processing—remains valid for any type of array-based surveillance radar system.

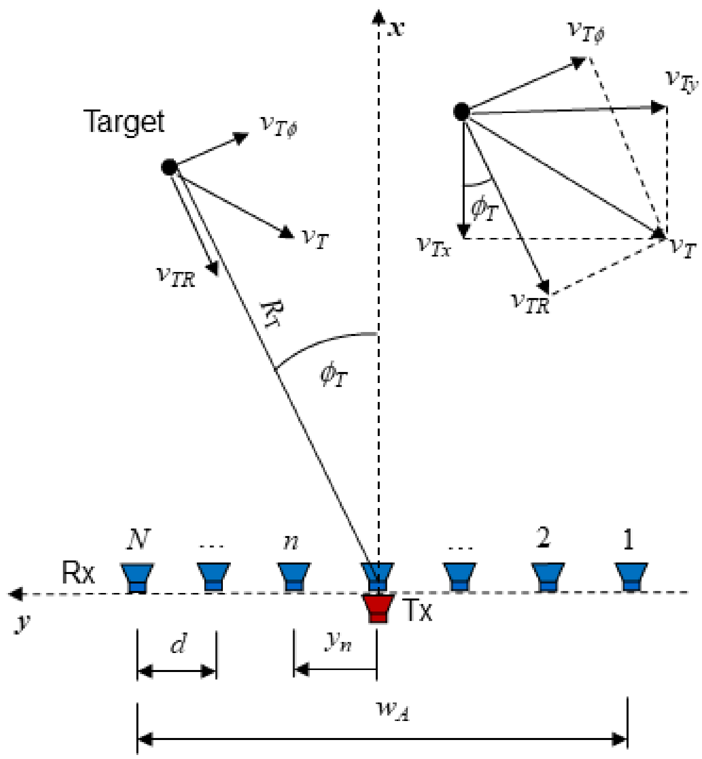

Fig. 1 Schematic representation of the surveillance AESA radar system equipped with a multistatic antenna array with one Tx in the middle

The analysis starts with establishing the point-target response (PTR) of a point target located at range R_T and azimuth ϕ_T with respect to the origin, moving with the velocity vector $\mathbf{v}_T$. The latter can be decomposed along the Cartesian axes into the $\left(v_{Tx}, v_{Ty}\right)$ components or the polar axes into the $\left(v_{TR}, v_{T\phi}\right)$ components (see Fig. 1). We assume the radar signal samples are functions of the discrete variables frequency (f_l), slow time (t_m), and array position (y_n). The frequency f_l spans the interval between $f_c - \dfrac{B}{2}$ and $f_c + \dfrac{B}{2}$ (where f_c is the carrier frequency and B is the bandwidth), the slow time sample t_m (which represents the onset time of the m^{th} pulse in the train of M pulses) goes from $-\dfrac{T_{CPI}}{2}$ to $\dfrac{T_{CPI}}{2}$ (where T_{CPI} is the duration of the coherent processing interval [CPI]), and the array position y_n varies from $-\dfrac{w_A}{2}$ to $\dfrac{w_A}{2}$. With these provisions, the PTR can be written as follows:

$$\mathrm{PTR}\left(f_l, t_m, y_n; R_T, \phi_T, \mathbf{v}_T\right) =$$
$$\exp\left[-j\frac{2\pi f_l}{c}\left(\begin{array}{l}\sqrt{\left(R_T\cos\phi_T - v_{Tx}t_m\right)^2 + \left(R_T\sin\phi_T - v_{Ty}t_m\right)^2} + \\ \sqrt{\left(R_T\cos\phi_T - v_{Tx}t_m\right)^2 + \left(R_T\sin\phi_T - v_{Ty}t_m - y_n\right)^2}\end{array}\right)\right]. \tag{1}$$

Note that we ignored any magnitude factors that may appear in the PTR formula. These magnitude factors would typically depend on frequency and range. The frequency variation is primarily dependent on the antenna element types and may only affect the PTR magnitude in systems operating with very large fractional bandwidths. The range has a significant impact on the PTR magnitude only in systems working at close ranges, which are outside the scope of this investigation.

By using the identities $v_R = v_x\cos\phi + v_y\sin\phi$ and $v^2 = |\mathbf{v}|^2 = v_x^2 + v_y^2$, we can recast the PTR as

$$\mathrm{PTR}\left(f_l, t_m, y_n; R_T, \phi_T, \mathbf{v}_T\right) =$$
$$\exp\left[-j\frac{2\pi f_l}{c}\left(\begin{array}{l}\sqrt{R_T^2 - 2R_T v_{TR} t_m + v_T^2 t_m^2} + \\ \sqrt{R_T^2 - 2R_T v_{TR} t_m + v_T^2 t_m^2 - 2R_T y_n\sin\phi_T + 2v_{Ty}t_m y_n + y_n^2}\end{array}\right)\right]. \tag{2}$$

The RM is created via a multidimensional matched filter, which takes in the radar measurement in the frequency, slow time, and array position dimensions and transforms it into a map in the range, velocity, and azimuth angle dimensions. Let $S\left(f_l, t_m, y_n\right)$ be the baseband radar received signal at frequency f_l, slow time t_m, and array position y_n. Then, the RM at range R, velocity $\mathbf{v}$, and azimuth ϕ is obtained by correlating the radar signal with the conjugate of the PTR of a hypothetical point target placed at coordinates $\left(R, \phi, \mathbf{v}\right)$.

$$\mathrm{RM}\left(R, \phi, \mathbf{v}\right) = \sum_l\sum_m\sum_n S\left(f_l, t_m, y_n\right)\mathrm{PTR}^*\left(f_l, t_m, y_n; R, \phi, \mathbf{v}\right) =$$
$$\sum_l\sum_m\sum_n S\left(f_l, t_m, y_n\right)\exp\left[j\frac{2\pi f_l}{c}\left(\begin{array}{l}\sqrt{R^2 - 2Rv_R t_m + v^2 t_m^2} + \\ \sqrt{\begin{array}{l}R^2 - 2Rv_R t_m + v^2 t_m^2 - \\ 2Ry_n\sin\phi + 2v_y t_m y_n + y_n^2\end{array}}\end{array}\right)\right]. \tag{3}$$

At this point, we need to discuss the fact that, as well-known in radar Doppler processing theory, a system such as that described in Fig. 1 only allows the estimation of the target's radial velocity component v_{TR}, but not of its transversal velocity component $v_{T\phi}$.[1] Although, in principle, we could formally develop a matched filter that generates a 4-D RM of coordinates $\left(R, \phi, v_R, v_\phi\right)$, the resolution in the v_ϕ dimension would be extremely poor. For that reason, our objective is to limit the RM to only three dimensions (R, ϕ, v_R). Nevertheless, a complete characterization of the target's dynamic state should include R_T, ϕ_T, v_{TR}, and $v_{T\phi}$; the transversal velocity component $v_{T\phi}$, which cannot be estimated directly from the radar measurement in this configuration, is typically evaluated by the radar system in tracking mode.[1] In subsequent paragraphs, we discuss the conditions under which this velocity component can be ignored in the RM formation processing scheme.

From a computational standpoint, implementing the formula in Eq. 3, which represents the exact, brute-force matched filter, is a very inefficient process. Assuming we have L frequency samples, M slow-time samples, and N array elements, while the RM contains L, M, and N discrete "bins" in range, velocity, and azimuth, respectively, the map formation described by Eq. 3 is an $O\left(L^2 M^2 N^2\right)$ procedure. This computational complexity is, in most cases, unacceptable for a radar system that is supposed to work in real time.

By contrast, the conventional processing in most low-resolution AESA systems can be described by the following equation:

$$\mathrm{RM}\left(R, \sin\phi, v_R\right) = \sum_l \sum_m \sum_n S\left(f_l, t_m, y_n\right) \exp\left[j \frac{4\pi}{c} \left(f_l R - f_c t_m v_R - \frac{f_c}{2} y_n \sin\phi \right) \right]. \quad (4)$$

The expression within the exponential function suggests that the formula Eq. 4 can be implemented as a 3-D DFT from $S\left(f_l, t_m, y_n\right)$ to $\mathrm{RM}\left(R, \sin\phi, v_R\right)$, using the Fourier variable pairs (f, R), (t, v_R), and $(y, \sin\phi)$, with some appropriate scaling factors. (Note that, to evidence the Fourier transform structure in all three dimensions, we replaced ϕ by $\sin\phi$.) Since the formula in Eq. 4 can be efficiently implemented via a 3-D FFT, the computational complexity is reduced to $O\left(LMN \log_2 LMN\right)$, which makes it more amenable to a real-time operation of the radar system.

One should note that practical implementations of an AESA radar system do not always directly use a 3-D FFT approach to the RM formation, as described by Eq. 4. In many cases, the pulse compression, Doppler processing, and beamforming are implemented in hardware via analog or digital filters (in the case of pulse compression and Doppler processing) and phase shifters (in the case of beamforming).[1] In addition, the signal digitization and pulse compression can be done directly in the (fast) time domain, without transitioning to the frequency domain. However, one can conceive a practical radar system where these operations are performed exactly as in Eq. 4, by an on-board computer. This is usually the case when digital pulse compression and digital beamforming on receive are used.[1] Note that many digital pulse compression schemes operate with samples in the frequency domain at some stage of the processing, which justifies our formulation starting with the radar signal samples as a function of frequency (instead of fast time). In addition, the frequency domain formulation facilitates the mathematical developments in the subsequent sections of this report.

The essential feature of the formula in Eq. 4 is that the Fourier variable pairs, (f, R), (t, v_R), and $(y, \sin\phi)$, appear within separate terms in the exponential function. In other words, the transform from the (f, t, y) space to the (R, ϕ, v_R) space is separable and can be efficiently implemented as a 3-D FFT. Note that the same feature is not available in Eq. 3, which precludes the direct application of FFT processing in that case. In the following, we say that the variables (f, t, y) are uncoupled when they appear in separate terms (as in Eq. 4) and coupled when the separation is not possible (as in Eq. 3).

As we demonstrate in Section 2.2, the formula in Eq. 4 can be obtained from Eq. 3 by making a series of approximations. These approximations are generally valid when the radar system operates with low resolution in all dimensions. When we try to increase the resolution in one or multiple dimensions past certain limits, we find that the decoupling of the radar signal variables becomes untenable and the direct application of the formula in Eq. 4 leads to defocusing errors in the RM formation.

2.2 Approximations to the Exact Matched Filter

The first approximation consists of neglecting the terms $v^2 t_m^2$ and $2 v_y t_m y_n$ under the square roots in Eq. 3. These are reasonable assumptions when we operate at long ranges and with a relatively short CPI. We can establish quantitative relationships between the radar system parameters under which these approximations are acceptable. Thus, if we rewrite the second square root in Eq. 3 using the first-order binomial expansion $\sqrt{1-a} \cong 1 - \frac{a}{2}$, we obtain

$$\begin{aligned}&\frac{2\pi f_l}{c}\sqrt{R^2 - 2R v_R t_m + v^2 t_m^2 - 2R y_n \sin\phi + 2 v_y t_m y_n + y_n^2} \cong \\ &\frac{2\pi f_l}{c}\left(R - v_R t_m + \frac{v^2 t_m^2}{2R} - y_n \sin\phi + \frac{v_y t_m y_n}{R} + \frac{y_n^2}{2R}\right)\end{aligned} \quad . \tag{5}$$

To limit the phase errors introduced by ignoring the third and fifth terms in this expression, we require that they are no larger than $\pi/4$ at the carrier frequency. Since we have $|t_m|^{\max} = \frac{T_{CPI}}{2}$ and $|y_n|^{\max} = \frac{w_A}{2}$, we obtain the inequalities

$$\frac{2\pi}{\lambda_c}\frac{v^2 T_{CPI}^2}{8R} \leq \frac{\pi}{4} \quad \text{and} \quad \frac{2\pi}{\lambda_c}\frac{v_y T_{CPI} w_A}{4R} \leq \frac{\pi}{4}, \tag{6}$$

which can also be written as

$$R \geq \frac{v^2 T_{CPI}^2}{\lambda_c} \quad \text{and} \quad R \geq \frac{2 v_y T_{CPI} w_A}{\lambda_c}, \text{ respectively,} \tag{7}$$

where λ_c is the wavelength at the carrier frequency. Since the Doppler and velocity resolutions are inverse proportional to T_{CPI}, it follows that imposing upper limits on the latter (as in Eq. 7) restricts the achievable resolutions in those dimensions.

Next, we consider neglecting the sixth term in Eq. 5. This implies that the array width is much smaller compared to the range of interest. To be more precise, if we limit the phase error introduced by ignoring that term to $\pi/8$ at the carrier frequency, we obtain

$$\frac{2\pi}{\lambda_c}\frac{w_A^2}{8R} \leq \frac{\pi}{8} \quad \text{or} \quad R \geq \frac{2 w_A^2}{\lambda_c}. \tag{8}$$

Note that this criterion is exactly the far-field condition familiar from antenna and antenna array theory.[6] In other words, neglecting the sixth term in Eq. 5 is equivalent to saying that the target is in the far-field region of the antenna array. When the inequality in Eq. 8 is not satisfied, we must deal with a near-field sensing scenario. Some possible approaches to deal with beamforming and Doppler processing in this situation were discussed in another publication.[7] Here, we observe that near-field conditions are typically associated with wide arrays, which in turn indicate high angular resolution. Therefore, imposing the far-field conditions on the radar sensing geometry implicitly limits the system's angular and cross-range resolutions.

Assuming the approximations discussed so far yield acceptable phase errors, the formula in Eq. 3 can be reduced to

$$\mathrm{RM}(R, \sin\phi, v_R) = \sum_l \sum_m \sum_n S(f_l, t_m, y_n) \exp\left[j \frac{4\pi}{c}\left(f_l R - f_l t_m v_R - \frac{f_l}{2} y_n \sin\phi \right)\right]. \tag{9}$$

This equation is similar with Eq. 4, with the exception that the f_l factor appears in the second and third terms instead of f_c. To make the transition from Eq. 9 to Eq. 4, we need to introduce the narrowband assumption ($f_l \cong f_c$) for those two terms, but not for the first one. A narrowband radar system is associated with low-range resolution; however, this condition appears essential in achieving the decoupling of dimensions in the sense described in Section 2.1.

So far, we have shown that the approximations necessary to obtain decoupled radar measurement dimensions impose limits on the system's parameters (bandwidth, array width, and CPI duration), with negative consequences in terms of the achievable resolutions in the three dimensions of the RM. In the following section, we present a quantitative discussion of the coupling conditions between each dimension pairs (range-Doppler, azimuth-Doppler, and range-azimuth, respectively), as well as possible signal processing approaches for the coupled dimension cases.

2.3 Range-Doppler Coupling

An efficient sequence in the signal processing chain for RM formation of a radar system described in Fig. 1 consists of the following:

1) Create range-Doppler maps (RDMs) at each array element, independently from one another.
2) Select the Doppler bins that contain detection hits, within the velocity ranges characterizing the targets of interest. This selection should be done by a coincidence rule (e.g., the RDMs for most of array elements show positive detections in the same Doppler bin).
3) Create range-azimuth maps (RAMs) for each Doppler bin selected by the rule outlined in the previous step.

In this section, we discuss the range-Doppler coupling issue, which is the easiest to explain and handle by signal processing algorithms. Since the RDMs can be created independently at each array element, the mapping problem in this case is reduced to two dimensions. For each of the RDMs, the range origin is set to the location of the Rx corresponding to the current array element (which is different from the global range origin shown in Fig. 1, in the array's center).

The range-Doppler coupling may take place in a high-resolution radar system due to the target migration through range resolution cells during a CPI and was analyzed in detail in previous work.[8] The phenomenon is illustrated graphically in Fig. 2: this occurs when the radial distance traveled by the target during a CPI, $v_R T_{CPI}$, exceeds the range resolution δR. The conditions to avoid this from happening (or the range-Doppler decoupling conditions) can be stated, equivalently, as follows:

- The target must stay in the same range bin for all slow-time samples during a CPI; or
- The target must stay in the same Doppler bin at all frequencies in the radar signal spectrum.

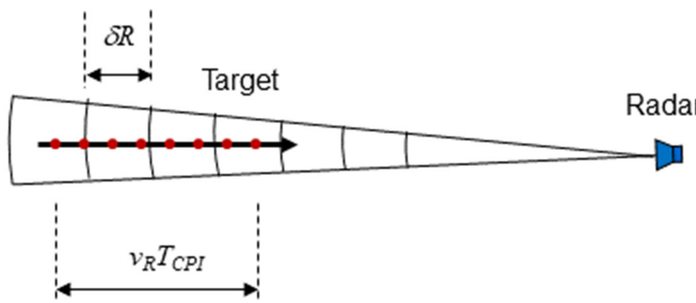

Fig. 2 Illustration of the target migration across multiple range resolution cells in a high-range resolution system operating with long CPI

The first condition can be written as $v_R T_{CPI} < \delta R$. Since the velocity resolution is $\delta v = \dfrac{\lambda_c}{2T_{CPI}}$, we obtain

$$\delta v \delta R > \frac{\lambda_c v_R}{2}. \tag{10}$$

In terms of bandwidth and CPI duration, the inequality becomes

$$BT_{CPI} < \frac{c}{2v_R}. \tag{11}$$

The alternative condition can be analyzed by computing the Doppler shifts at the ends of the radar frequency spectrum:

$$f_D^{\min} = \frac{2v_R f_{\min}}{c} \quad \text{and} \quad f_D^{\max} = \frac{2v_R f_{\max}}{c} \quad . \tag{12}$$

The statement in the second condition can be formally written as $f_D^{\max} - f_D^{\min} < \delta f_D = \dfrac{1}{T_{CPI}}$, where δf_D is the Doppler frequency resolution. Since we have $f_{\max} - f_{\min} = B$ and $\delta R = \dfrac{c}{2B}$, we can manipulate the previous inequality to obtain an expression identical to Eq. 10.

The inequality in Eq. 10 clearly indicates that we cannot simultaneously improve both the range and Doppler resolutions (which means reducing the $\delta v \delta R$ product) past certain limits without introducing coupling between the two dimensions in the processing. When the inequality in Eq. 10 is satisfied, the RDM can be created by a 2-D FFT of the radar data from the (f,t) domain to the (R,v_R) domain. When that condition does not hold, a more complex approach to the RDM formation is required, as outlined in the following paragraphs.

To develop a general algorithm for RDM formation, we first assume we can perform an expansion as in Eq. 5 and neglect the $\frac{2\pi}{\lambda_c}\frac{v^2 t_m^2}{2R}$ term (note that all terms containing y_n are irrelevant to this step in the processing), and we obtain

$$\mathrm{RDM}(R,v_R)=\sum_l\sum_m S(f_l,t_m)\exp\left[j\frac{4\pi}{c}(f_l R - f_l t_m v_R)\right]. \tag{13}$$

In the narrowband regime, we can approximate $f_l \cong f_c$ in the second term of the exponential's argument and obtain the conventional range-Doppler processing scheme, which consists of a 2-D FFT between the (f,t) and (R,v_R) variable pairs.

In the wideband regime, the frequency and slow-time variables are coupled due to the presence of the term $f_l t_m v_R$ in the exponential in Eq. 13. This means we cannot directly apply a 2-D FFT to compute the expression in the right side. However, the RDM computations can still be performed via a 2-D FFT in this case, if we use the Keystone transform of the data as an intermediate step.[9] This consists of interpolating the radar samples from a uniform rectangular grid in the (f,t) space to a uniform rectangular grid in the (f,t^k) space, where

$$t^k = t\frac{f}{f_c}. \tag{14}$$

Subsequently, the data processing from the (f,t^k) domain to the (R,v_R) domain can be performed as a 2-D FFT. The efficiency of this algorithm is very close to that of the conventional range-Doppler processing scheme, meaning the coupling between the range and Doppler dimensions should not affect the radar system's overall processing speed in any significant way. More details on the RDM formation algorithm based on the Keystone transform can be found in Dogaru[8] and are not repeated in the current report.

2.4 Azimuth-Doppler Coupling

The ability to perform step 2 in the processing sequence outlined in Section 2.3 hinges on the assumption that a target is present in the same Doppler bin within the RDMs obtained at all array elements. In the contrary case, we say that the azimuth and Doppler dimensions are coupled—this significantly increases the complexity of radar processing, which now cannot be performed as a sequence of 2-D map formation procedures, but it would need to be carried out directly in 3-D.

We can state the condition of azimuth and Doppler decoupling in two equivalent forms:

1) The target must stay in the same array beam (or azimuth resolution bin) for all slow-time samples during a CPI; or

2) The target must stay in the same Doppler bin at all array elements.

The first condition, which avoids the target migration through array beams during a CPI (as illustrated in Fig. 3), can be written as $v_\phi T_{CPI} < R\delta\phi$, where $\delta\phi = \dfrac{\lambda_c}{w_A \cos\phi}$ is the azimuth angular resolution (or the array beamwidth). Using the expression for radial velocity resolution $\delta v = \dfrac{\lambda_c}{2T_{CPI}}$ we obtain

$$\delta v \delta\phi > \frac{\lambda_c v_\phi}{2R}. \tag{15}$$

In terms of array width and CPI duration, the inequality becomes

$$w_A T_{CPI} < \frac{\lambda_c R}{v_\phi}. \tag{16}$$

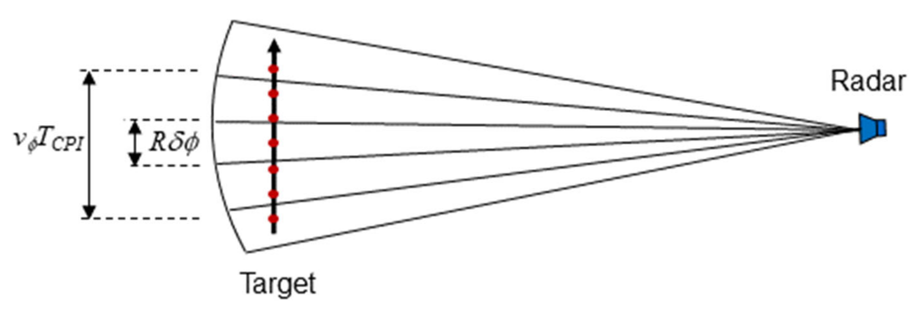

Fig. 3 Illustration of the target migration across multiple radar array beams in a high-range resolution system operating with long CPI

Analyzing the second condition requires a more elaborate treatment but leads to the same relationship as in Eq. 15. This inequality shows that we cannot simultaneously increase the Doppler and angular resolutions past certain limits without introducing coupling between these dimensions.

It is interesting to note that, if we plug in the expressions for $\delta\phi$ and δv in Eq. 15 and rearrange the two sides, we obtain

$$R > \frac{v_\phi \cos\phi T_{CPI} w_A}{\lambda_c}, \tag{17}$$

which is clearly reminiscent of the second inequality in Eq. 7 (with the exception that $v_y \cong v_\phi \cos\phi$ only for small angles ϕ).

In the end, fulfilling all the conditions given by Eqs. 7, 10, and 15 comes down to limiting the CPI duration (T_{CPI}), which, in turn, limits the achievable Doppler resolution. High-resolution Doppler processing (long integration times) is typically only required for slow targets, for which we need to ensure a small minimum detectable velocity.[1] Since in all those inequalities T_{CPI} appears factored together with a velocity component (as in $v_R T_{CPI}$ or $v_\phi T_{CPI}$), the logical choice of short CPI for fast targets and long CPI for slow targets is, in most cases, enough to satisfy the decoupling conditions.

The case when the inequality in Eq. 15 is not satisfied and the azimuth and Doppler dimensions become coupled is the most difficult to handle from an algorithmic point of view. In that scenario, the conditions in Eq. 7 are likely not met either, which rules out some of the simplifications to the exact matched filter formula (Eq. 3) performed in Section 2.2. Moreover, even if we tried to implement the exact 4-D-matched filter in Eq. 3, one major problem is that we cannot obtain a good estimate of the transversal velocity component (either v_ϕ or v_y) directly from the radar measurement. That velocity component would have to be estimated outside of the RM formation procedure (e.g., in the radar tracking mode) and then plugged into the expression in Eq. 3.

Currently, we are not aware of any efficient algorithm that can handle the azimuth-Doppler coupling problem in AESA-based radar systems. Some possible approaches may be borrowed from the techniques used in SAR imaging of moving targets.[10] These should be the subject of future investigations. For the time being, it is far more preferable to deal with a sensing scenario in which the azimuth and Doppler dimensions are uncoupled and one can simply ignore the transversal velocity component in the RM formation.

2.5 Range-Azimuth Coupling

To analyze the range-azimuth coupling problem, we assume that the first two steps in the sequence indicated in Section 2.3 were completed, and our objective is to create 2-D RAMs in each Doppler bin at a time, where targets were detected. Since the Doppler processing compensates for the target motion, each RAM is created with the target "frozen" at its location in the middle of the CPI.

In narrowband radar systems, the range resolution is poor, and we typically assume that all array elements see the target in the same resolution cell: this is what we call the uncoupled range-azimuth case. However, when the radar operates with wideband waveforms (fine range resolution), the target may appear in different range bins to different array elements: this is the range migration phenomenon, which is frequently encountered in radar imaging. A graphic illustration of this phenomenon, contrasting the narrowband and wideband cases, is shown in Fig. 4.

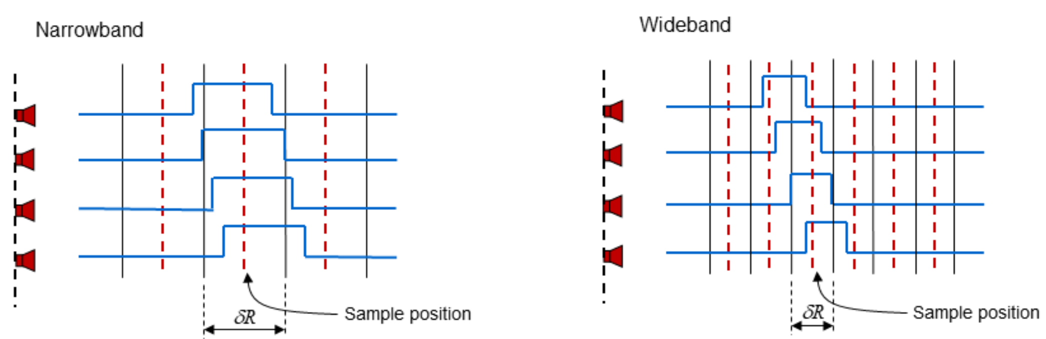

Fig. 4 Illustration of the target migration through multiple range resolution cells as we move across the array elements. The diagram emphasizes the difference between the narrowband case (where the fast-time sample "catches" the target return at each array node) and the wideband case (where the fast-time sample falls outside the target return at some array nodes).

The range-azimuth decoupling condition can be stated in one of the two following equivalent forms:

1) All the array elements must see the target in the same range bin; or

2) The target is in the same array beam at all frequencies within the radar signal spectrum.

To satisfy the first condition, we require that

$$R_1 - R_N < \delta R, \tag{18}$$

where $R_1 \cong R + \frac{w_A}{4}\sin\phi$ and $R_N \cong R - \frac{w_A}{4}\sin\phi$ are the target ranges measured at the two end elements of the array. Combining this with the expression of the angular resolution $\delta\phi = \frac{\lambda_c}{w_A \cos\phi}$, we obtain

$$\delta R \delta\phi > \frac{\lambda_c \tan\phi}{2}, \tag{19}$$

or, in terms of bandwidth and array width,

$$B w_A < \frac{c}{\sin\phi}. \tag{20}$$

Solving for the second condition involves more laborious steps, but the final result is identical to that in Eq. 19. This inequality shows that we cannot simultaneously increase both range and angular resolutions without introducing coupling between the two dimensions.

To perform the signal processing in array-based radar systems operating with wideband waveforms, wideband-beamforming techniques have been developed.[1] The traditional way of implementing these techniques consists of inserting time delay units (TDUs) at the output of each receiver element, with each unit introducing a delay proportional to the element's position in the array. This approach improves upon the basic implementation of beamforming using phase shifters, in which the steering angle of the beam displays unwanted variations with the radar signal's frequency. However, the conventional TDU approach to wideband beamforming is designed to work in the far-field region of the array and under the assumption of no coupling between range and azimuth dimensions.

In this section, we describe a wideband-beamforming algorithm meant to create the RAM in the most general case. We start by adapting Eq. 3 to the case of a stationary target:

$$\begin{aligned}\mathrm{RAM}(R,\phi) &= \sum_l \sum_n S(f_l, y_n) \exp\left[j \frac{2\pi f_l}{c}\left(R + \sqrt{R^2 - 2Ry_n \sin\phi + y_n^2} \right) \right] \\ &= \sum_n \sum_l S(f_l, y_n) \exp\left(j \frac{2\pi f_l}{c} R_n \right)\end{aligned}. \tag{21}$$

To simplify the notations, we introduced the symbol R_n designating the round-trip range from the current pixel at coordinates (R,ϕ) to the n^{th} array element. This round-trip range (R_n) corresponds to twice the range R that appears in Eq. 13, describing the RDM formation at array element index n (note that the symbols R in

Eqs. 13 and 21 have different meanings, because they are referenced to different coordinate system origins). The sum over the index l can be interpreted as the inverse DFT of the radar signal with respect to the frequency, computed at the time sample $\frac{R_n}{c}$. Therefore, we can write

$$\mathrm{RAM}(R,\phi) = \sum_n s_n\left(\frac{R_n}{c}\right), \tag{22}$$

where $s_n\left(\frac{R_n}{c}\right)$ is the range profile corresponding to array element index n, sampled at the time delay $\frac{R_n}{c}$. The set of N range profiles (one for each array element), corresponding to the Doppler bin selected for handling a given target, is readily available from the RDM formation step in the processing chain.

The expression in Eq. 22 essentially describes the time-domain backprojection algorithm (BPA),[3] which is widely used within the radar imaging community. In imaging applications, where the radar map is typically constructed in an (x,y) Cartesian coordinate frame, we write

$$R_n = \sqrt{x^2+y^2} + \sqrt{x^2+(y-y_n)^2}\ . \tag{23}$$

The BPA is highly versatile and can handle arbitrary sensing scenarios, including near-field, range-azimuth coupled, multistatic, and irregularly sampled arrays. Nevertheless, the algorithm is not particularly efficient from a computational standpoint, since the sum in Eq. 22, which needs to be performed for each pixel of the map, cannot be implemented via FFT techniques.

In another publication,[7] we developed an FFT-based algorithm that can perform beamforming with near-field arrays, for the uncoupled range-azimuth case. However, we were not able to extend that algorithm to the coupled range-azimuth scenario, when the map is created in polar coordinates. In fact, one may question the practical usefulness of a high-resolution radar map covering a very wide area in polar coordinates. A more sensible approach to high-resolution map creation is to zoom in on a small area of interest within a wide-area, low-resolution map. In this case, the differences between images formed on Cartesian and polar coordinate grids become minor and we can then apply highly efficient (FFT-based) imaging techniques such as the range migration algorithm,[3,4] which are designed to work with Cartesian coordinate pixel maps.

3. Numerical Examples

The numerical examples in this section are meant to illustrate the theory in Section 2. The radar parameters do not characterize any particular system currently in operation. Although some of the sensing scenarios presented here may seem contrived, they are specifically designed to evidence the coupling issues discussed so far in this report. We also keep things generic in terms of radar targets, by investigating the mapping of point targets.

3.1 Range-Doppler Coupling

To illustrate the range-Doppler coupling, we consider the RDM formation at one of the array elements of the radar system in Fig. 1. Since the RDMs are created independently for each array element, we can simply investigate a single-antenna radar system operating in monostatic configuration. For our numeric example, we pick a carrier (center) frequency f_c = 3 GHz (in the S-band) and a bandwidth B = 300 MHz. The CPI duration is T_{CPI} = 20 ms, with a pulse repetition frequency (PRF) = 6.4 kHz. We consider a point target placed at a range R_T = 10 km moving towards the radar with a radial velocity v_{TR} = 120 m/s. A quick evaluation indicates that we do not meet the inequality in Eq. 11, meaning that the target moves through several range resolution cells during a CPI, and the range and Doppler dimensions are coupled.

The conventional range-Doppler processing is described by

$$\mathrm{RDM}\left(R, v_R\right) = \sum_l \sum_m S\left(f_l, t_m\right) \exp\left[j \frac{4\pi}{c} \left(f_l R - f_c t_m v_R \right) \right]. \tag{24}$$

The result of applying this algorithm (which essentially implements a 2-D FFT) to the radar-sensing scenario outlined in the previous paragraph is displayed in Fig. 5a. When we apply the range-Doppler algorithm based on the Keystone transform (Eq. 13), we obtain the RDM in Fig. 5b. The latter map is clearly better focused than the first one, showing that the Keystone transform-based procedure yields superior results for the coupled range-Doppler case. Based on the radar system parameters, the theoretical resolution should be approximately 1 m in range and 4 m/s in velocity. (Note that we applied Hamming windows to the radar data in both dimensions.) The RDM in Fig. 5b reaches the theoretical resolutions, whereas the point-target "image" in Fig. 5a spreads out beyond those limits. In addition, there is a loss of 3.6 dB in the peak magnitude of the image in Fig. 5a compared to that in Fig. 5b. The reduction in peak magnitude of the point-target image has a negative impact on the SNR and detection performance of the radar system.

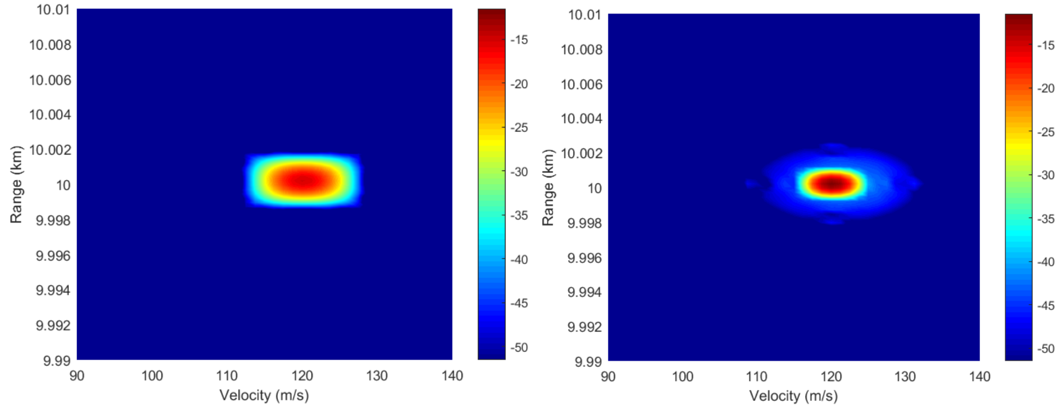

(a) (b)

Fig. 5 RDM of a point target at 10-km range, moving with radial velocity of 120 m/s, obtained by a) conventional range-Doppler processing (Eq. 24) and b) range-Doppler processing via the Keystone transform (Eq. 13)

3.2 Range-Azimuth Coupling

For the example demonstrating the range-azimuth coupling, we examine the radar system in Fig. 1 in the presence of a stationary target. As discussed before, the radar operates with a carrier frequency f_c = 3 GHz and a bandwidth B = 300 MHz. The ULA width is w_A = 50 m, made of N = 500 elements. Note that this array configuration allows unambiguous azimuth mapping up to ±30°, at 3 GHz. The stationary point target is placed at a range R_T = 1 km and an azimuth bearing ϕ_T = 20°. As in the previous numerical example, we apply Hamming windows to both radar data dimensions. This yields approximate resolutions of 1 m in range and 0.2° in azimuth. Inspecting these radar system parameters leads to concluding that the inequalities in Eqs. 19 and 20 are not satisfy; therefore, the range and azimuth dimensions are coupled.

A simple-minded RAM formation procedure consists of a 2-D FFT from the frequency-array position domain to the range-azimuth domain:

$$\mathrm{RAM}\left(R,\sin\phi\right)=\sum_{l}\sum_{n}S\left(f_l,y_n\right)\exp\left[j\frac{4\pi}{c}\left(f_lR-\frac{f_c}{2}y_n\sin\phi\right)\right]. \tag{25}$$

This approach to the RAM creation yields the result in Fig. 6a. The rigorous imaging procedure described by Eq. 22 (equivalent to the BPA) generates the map in Fig. 6b. The difference between the two point-target images is obvious. While the image in Fig. 6b is well focused and reaches the theoretical resolution, the one in Fig. 6a is spread out beyond the resolution limits and incurs a 14-dB reduction in peak magnitude compared to the correctly focused counterpart. One should note that the range migration issue in this sensing scenario is compounded by the fact that the algorithm described by Eq. 25 does not account for the near-field geometry, which explains the very poor resolution obtained in Fig. 6a.

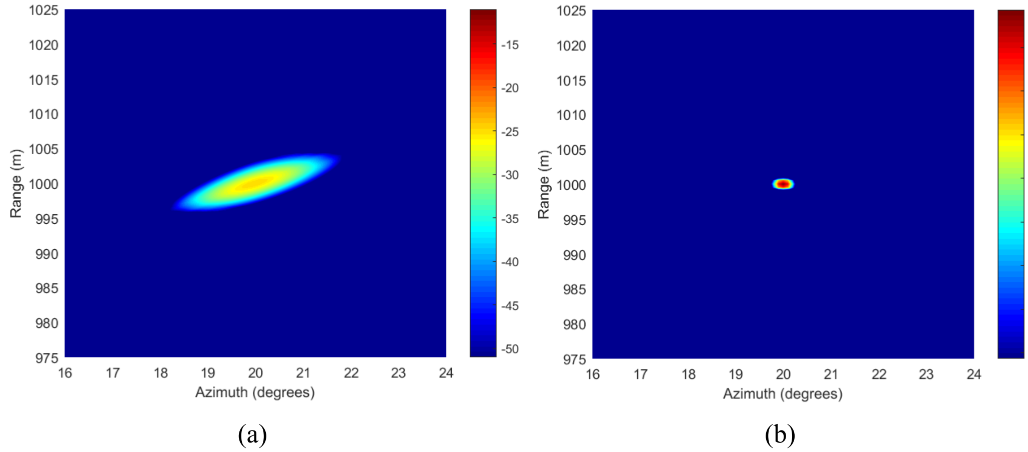

Fig. 6 RAM of a stationary point target located at 1-km range and 20° azimuth, obtained by a) 2-D FFT processing of radar data in frequency-array position domain (Eq. 25) and b) processing by BPA (Eq. 22)

3.3 Azimuth-Doppler Coupling

The key question we want to investigate in relation to the azimuth-Doppler coupling issue is whether a large transversal velocity component of the target $v_{T\phi}$ impacts the quality of the RM. As previously mentioned, this velocity component cannot be directly estimated by measurements with the radar system described in Fig. 1 operating in search mode. Therefore, it is interesting to study the effect of $v_{T\phi}$ on the RM in the case when such an estimate is available, as well as in the case when we simply ignore this velocity component in the RM formation algorithm.

We first focus our attention on the Doppler-azimuth map (DAM) generation in an array-based system operating at a single frequency, f_c = 3 GHz. We use the same radar parameters as in the previous two sections: the ULA width is w_A = 50 m, made of N = 500 elements, and the CPI duration is T_{CPI} = 20 ms, with PRF = 6.4 kHz. The target is placed at a range R_T = 1 km and an azimuth bearing ϕ_T = 20°, while its velocity vector has the following components: v_{TR} = 30 m/s and $v_{T\phi}$ = 200 m/s. A quick inspection of these parameters indicates that the azimuth and Doppler dimensions are coupled (the inequality in Eqs. 15 and 16 are not satisfied).

The most basic form of DAM formation implements a 2-D FFT from the slow time-array position domain to the Doppler-azimuth domain:

$$\mathrm{DAM}\left(v_R, \sin\phi\right) = \sum_m \sum_n S\left(t_m, y_n\right) \exp\left[-j\frac{4\pi f_c}{c}\left(t_m v_R + \frac{y_n \sin\phi}{2}\right)\right]. \tag{26}$$

We compare the results obtained by this procedure with those generated by the exact matched filter, under the assumption that we have the correct estimate of both R_T and v_{Ty} ("the best-case scenario"):

$$\mathrm{DAM}\left(v_R,\phi\right)=\sum_m\sum_n S\left(t_m,y_n\right)\exp\left[j\frac{2\pi f_c}{c}\left(\sqrt{R_T^2-2R_Tv_Rt_m+v_T^2t_m^2}+\sqrt{\begin{array}{l}R_T^2-2R_Tv_Rt_m+v_T^2t_m^2-\\2R_Ty_n\sin\phi+2v_{Ty}t_my_n+y_n^2\end{array}}\right)\right]. \quad (27)$$

One should note that the terms $v^2t_m^2$ are practically always negligible and can be safely ignored in the matched filter formula, so only the v_{Ty} prior estimate is required by this procedure.

The DAMs obtained in the presence of the point target are displayed in Fig. 7a (for the approximate procedure in Eq. 26) and in Fig. 7b (for the exact procedure in Eq. 27). The image in Fig. 7b is correctly focused and reaches the theoretical resolution, whereas the one in Fig. 7a is poorly focused in the azimuth dimension and its peak magnitude drops by 5 dB below that of the correct image.

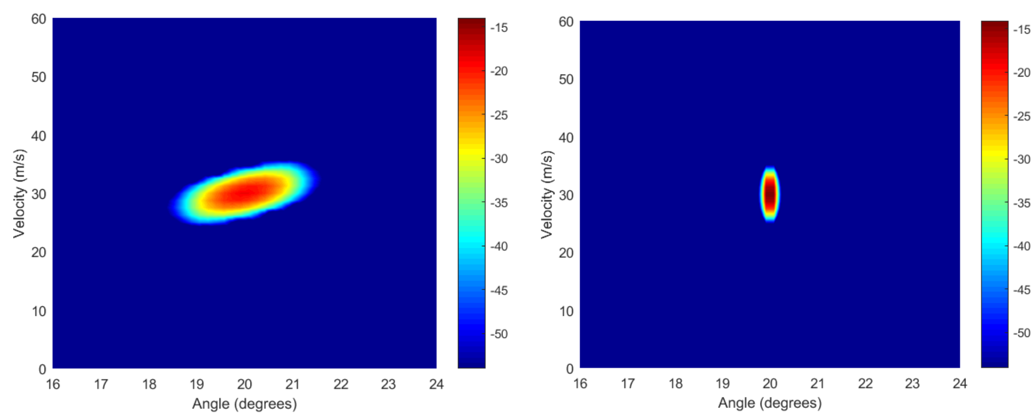

(a) (b)

Fig. 7 DAM of a stationary point target located at 1-km range and 20° azimuth, moving with v_{TR} = 30 m/s and $v_{T\phi}$ = 200 m/s, obtained by a) 2-D FFT processing of radar data in slow time-array position domain (Eq. 26) and b) the exact matched filter (Eq. 27)

However, it turns out that the lack of azimuth focusing displayed by the image in Fig. 7a is not the result of the large transversal velocity component of the target, but of the fact that Eq. 26 does not consider the near-field character of the sensing geometry (see Eq. 8). To prove this, we perform two additional simulations. In the first one (Fig. 8a), we keep the processing by Eq. 26, but in the presence of no transversal velocity component ($v_{T\phi}$ = 0). As clearly seen in Fig. 8a, the azimuth defocusing is still present in this case. In the second simulation (Fig. 8b), we reintroduce the transversal velocity component ($v_{T\phi}$ = 200 m/s), but we use a modified version of Eq. 26 that implements a phase correction for the near-field array sensing geometry[7]:

$$\mathrm{DAM}\left(v_R,\phi\right)=\sum_m\sum_n S\left(t_m,y_n\right)\exp\left[-j\frac{4\pi f_c}{c}\left(t_m v_R+\frac{y_n\sin\phi}{2}-\frac{y_n^2\cos^2\phi}{4R_T}\right)\right]. \quad (28)$$

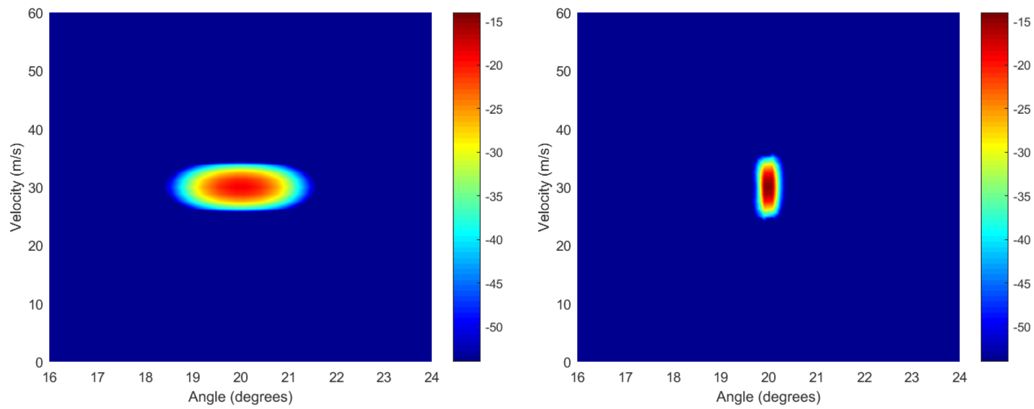

(a) (b)

Fig. 8 DAM of a stationary point target located at 1-km range and 20° azimuth, moving with v_{TR} = 30 m/s, obtained by the following: a) 2-D FFT processing of radar data in slow time-array position domain (Eq. 26), in the absence of a transversal velocity component; and b) the approximate matched filter described by Eq. 28, in the presence of a transversal velocity component ($v_{T\phi}$ = 200 m/s)

The image in Fig. 8b is almost as well focused as that in Fig. 7b, with only a slight loss of resolution in the radial velocity dimension. Note that the formula in Eq. 28 does not require an estimate of v_{Ty}, and, as shown by Dogaru and Ranney,[7] errors in the target range estimate have a very small impact on the DAM focusing. These results are somewhat surprising, because they seem to suggest that a large transversal velocity component of the target (and implicitly the presence of the azimuth-Doppler coupling) does not have a significant impact on the RM quality.

We take the analysis further by completing the entire 3-D RM three-step formation procedure, outlined in the beginning of Section 2.3. For this purpose, we simulate the operation of the system according to that sequence, by keeping the same parameters of the array and Doppler processing and, in addition, introducing a bandwidth B = 300 MHz. One should note that this scenario meets the coupling conditions among all three pairs of dimensions.

After creating the RDMs at each array element, we plot the Doppler profiles corresponding to the range bin of peak magnitude, as a function of the array element index. Figure 9a shows this plot for the case when the target has no transversal velocity component ($v_{T\phi}$ = 0). As expected, the target shows up in the same Doppler bin (index no. 89) at all array elements. In Fig. 9b, we display the same plot for the case when $v_{T\phi} = 200$ m/s. Now, the Doppler bin containing the target varies (from index nos. 91 to 87) across the array elements. This means we cannot unambiguously pick one Doppler bin representing the target radial velocity and use the data corresponding to that bin to create the RAM in step 3 of the procedure. This is a clear illustration of the azimuth-Doppler coupling, which can be stated as the target migration through Doppler bins across the array elements.

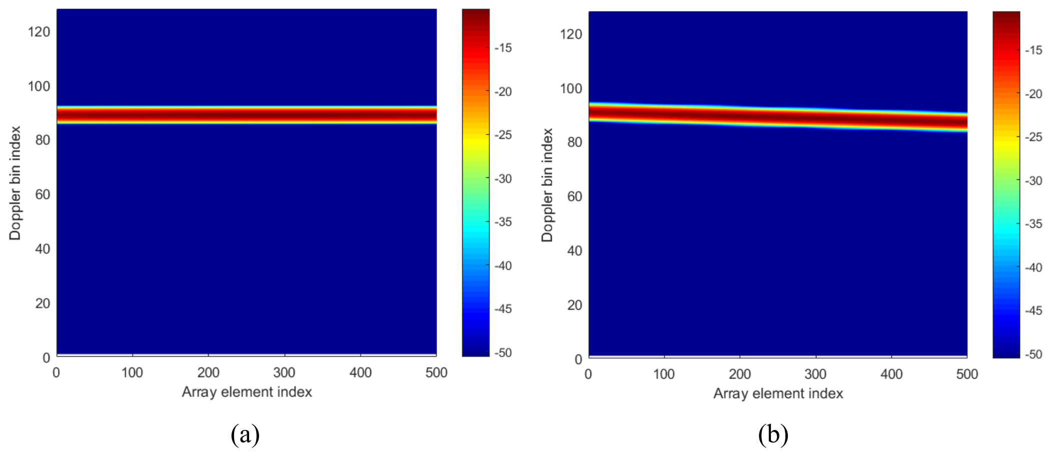

Fig. 9 2-D maps of the target position in the Doppler profiles across the array elements, for the cases a) $v_{T\phi} = 0$ and b) $v_{T\phi} = 200$ m/s

Nevertheless, when we compare the RAMs obtained in the two cases (Fig. 10), we notice a very small amount of defocusing of the target image in the presence of the large transversal velocity component (this is the case depicted in Fig. 10b). Moreover, the peak image magnitude reduction compared to the ideal case (Fig. 10a) is only 1 dB. Note that in both cases, we picked the range profiles from the same Doppler bin index (no. 89) across all array elements for processing via Eq. 22. This result reinforces the conclusion that, despite having to deal with the azimuth-Doppler coupling issue, the impact of a large transversal velocity component does not seem to have a major impact on focusing the high-resolution target image.

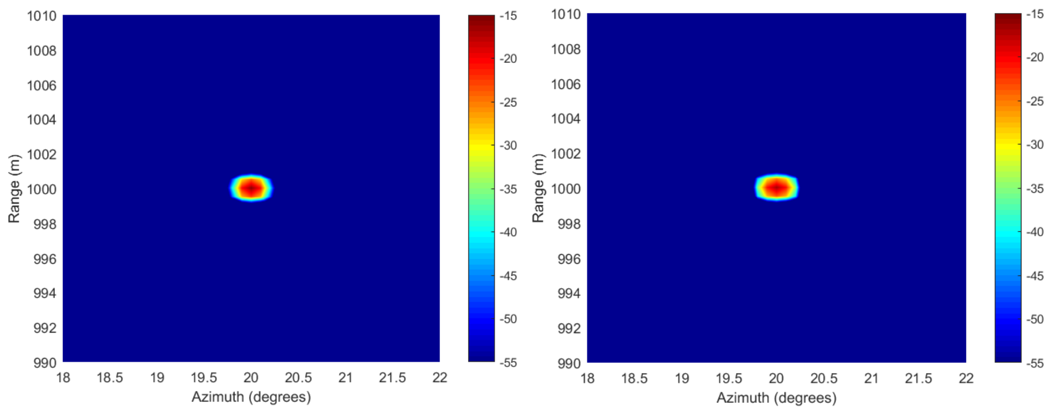

(a) (b)

Fig. 10 RAM of the point target obtained by simulating the AESA system operating by the procedure outlined in Section 2.3, when the target moves with the following transversal velocity components: a) $v_{T\phi} = 0$ and b) $v_{T\phi} = 200$ m/s

4. Conclusions

In this report, we explored some of the challenges related to attempting to generate a high-resolution RM with an AESA surveillance radar system operating in search mode. These systems traditionally work with relatively low spatial resolution primarily due to constraints on the antenna array size, whereas the signal processing involved in the RM formation can be described as a 3-D FFT from the frequency, array position, and slow time domain to the range, azimuth, and radial velocity domain. However, as we increase the system resolution in the three dimensions, the FFT-based processing, which relies on a series of approximations, introduces focusing errors in the RM. To alleviate these errors, a more accurate formulation of the matched filter is required, which typically results in slower processing times.

In Section 2, we established the exact formulation of the matched filter for the case of a target moving with arbitrary velocity vector and examined the conditions that permit this formulation to be simplified. We also determined the quantitative criteria that allow the pairs of radar measurement dimensions to decouple, that is, to enable FFT-like processing to generate an accurate radar map in those dimensions. One should note that the inequalities in Eqs. 10, 11, 15, 16, 19, and 20 do not necessarily establish some hard boundaries between the coupled and uncoupled regimes. Instead, the performance of the FFT-based processing scheme experiences a continuous degradation as we approach and eventually exceeds those relationships between the radar system parameters. Ultimately, the radar system designer must decide whether the phase errors characterizing the conventional processing, manifested as loss of resolution and target peak magnitude in the RM, are an acceptable tradeoff to the increase of computational complexity and processing time required by a more accurate implementation of the matched filter.

Signal processing algorithms for the coupled-dimension cases were discussed as well in Section 2. The range-Doppler processing can be treated with relatively little penalty in terms of speed, in the coupled scenario, via the Keystone transform. The range-azimuth coupled case, which is frequently encountered in high-resolution radar imaging, can be treated by the BPA. Although this algorithm is not particularly fast, quasi-real-time operation can be achieved if only a limited number of Doppler bins are processed. The azimuth-Doppler coupling issue is more difficult to tackle from an algorithmic standpoint; moreover, since the radar measurement does not allow a direct determination of the transversal velocity component of the target, this must be estimated by other means and plugged back into the matched filter formula.

Section 3 supports the theoretical developments with several simple numerical examples based on point targets. Each coupled dimensional pair is examined by computer simulations, by creating 2-D maps over the respective dimensions and comparing the 2-D FFT processing with the more advanced algorithms outlined in Section 2. The most surprising results were obtained when we introduced azimuth-Doppler coupling due to a large transversal velocity component of the target. The final RAM obtained in the Doppler bin characterizing the target displays very little defocusing compared to the ideal case (no transversal velocity component). This suggests that the azimuth-Doppler coupling may not have a significant impact on the overall RM formation procedure after all.

The results established in this report, particularly the algorithms that enable the RM formation by the three-step procedure outlined in Section 2.3, constitute the foundation for future investigations into high-resolution, multidimensional signal processing with AESA-based radar systems. In a subsequent publication, we plan to apply these techniques to more complex simulations, demonstrating their usefulness in realistic radar-sensing scenarios.

5. References

1. Richards M, Scheer J, Holm W. Principles of modern radar – basic principles. SciTech Publishing; 2010.
2. Taylor J, editor. Advanced ultrawideband radar: signals, targets, and applications. CRC Press; 2017.
3. Soumekh M. Synthetic aperture radar signal processing. Wiley; 1999.
4. Carrara W, Goodman R, Majewski R. Spotlight synthetic aperture radar. Artech; 1995.
5. Melvin W, Scheer J. Principles of modern radar – advanced techniques. SciTech Publishing; 2013.
6. Balanis C. Antenna theory–analysis and design. Wiley; 1997.
7. Dogaru T, Ranney K. Doppler processing with near-field arrays. Proc. SPIE. 2024;13048.
8. Dogaru T. Doppler processing with ultra-wideband (UWB) radar revisited. Army Research Laboratory (US); 2018 Jan. Report No.: ARL-TN-0866.
9. He Y, Molchanov P, Sakamoto T, Aubry P, Le Chevalier F, Yarovoy A. Range-Doppler surface: a tool to analyze human target in ultra-wideband radar. IET Rad Sonar Nav. 2015;9(9):1240–1250.
10. Soumekh M. Fourier array imaging. Prentice Hall; 1994.

List of Symbols, Abbreviations, and Acronyms

2-/3-/4-D	2-/3-/4-dimensional
AESA	active electronically scanned array
BPA	backprojection algorithm
CPI	coherent processing interval
DAM	Doppler-azimuth map
DFT	discrete Fourier transform
FFT	fast Fourier transform
PRF	pulse repetition frequency
PTR	point-target response
RAM	range-azimuth map
RDM	range-Doppler map
RM	reflectivity map
Rx	receiver
SAR	synthetic aperture radar
SNR	signal-to-noise ratio
TDU	time delay unit
Tx	transmitter
ULA	uniform linear array

1 (PDF)	DEFENSE TECHNICAL INFORMATION CTR DTIC OCA
1 (PDF)	DEVCOM ARL FCDD RLB CI TECH LIB